Nano Today 56 (2024) 102300

Contents lists available at ScienceDirect

Nano Today

journal homepage: www.elsevier.com/locate/nanotoday

Nano-bio interaction of magnetic nanoparticles with cells in a tumor at the single-cell level

Alexandra G. Pershina [a,b,*], Lina V. Efimova [a], Olga Y. Brikunova [a], Kseniya V. Nevskaya [a], Ekaterina V. Sukhinina [a,b], Ekaterina S. Hmelevskaya [a], Alexander M. Demin [c], Victor A. Naumenko [d], Dina Malkeyeva [e], Elena Kiseleva [e], Anna A. Khozyainova [f], Maxim E. Menyailo [f], Evgeny V. Denisov [f], Aleksey S. Volegov [g], Mikhail A. Uimin [h], Victor P. Krasnov [c], Ludmila M. Ogorodova [a]

[a] Center of Bioscience and Bioengineering, Siberian State Medical University, Russia
[b] Research School of Chemical and Biomedical Engineering, Tomsk Polytechnic University, Russia
[c] I. Ya. Postovsky Institute of Organic Synthesis, UB RAS, Russia
[d] V. P. Serbsky National Medical Research Center for Psychiatry and Narcology, Russia
[e] Institute of Cytology and Genetics, SB RAS, Russia
[f] Laboratory of Cancer Progression Biology, Cancer Research Institute, Tomsk National Research Medical Center, Russian Academy of Sciences, Russia
[g] Ural Federal University, Russia
[h] M. N. Miheev Institute of Metal Physics, UB RAS, Russia

ARTICLE INFO

Keywords:
Cancer
Magnetic nanoparticles
Nano-bio interaction
Distribution
Single-cell sequencing

ABSTRACT

A benefit of biomedical application of nanosystems is implementation of a precise effect at the level of an individual cell, and magnetic nanoparticles (MNPs) are some of the best candidates for the development of an intelligent nanosystem with remote control. To develop a nanosystem for precise therapy, a deep understanding of the nanosystem's *in vivo* behavior is required. Here, we studied penetration and distribution of PEGylated iron oxide MNPs unmodified or modified with the pH low insertion peptide (a ligand for smart targeting of the tumor acidic microenvironment) *in vivo* in a 4T1 mouse tumor. We revealed that MNPs penetrate into the tumor via both vascular burst and endothelial transcytosis. By implementing an approach based on single-cell high-throughput RNA sequencing, we identified the populations of the cells that took up MNPs in the 4T1 tumor and revealed preferential accumulation of MNPs in regulatory Trem2^{+} tumor-associated macrophages.

One of the most extensively studied applications is use of nanoparticles to treat cancer. Nanoparticles are extensively investigated as a vehicle for delivery of chemotherapeutics and as an agent for hyperthermia or photodynamic or photothermal therapy; thus, most of published research is focused on improving delivery efficiency. Nonetheless, probably only one strategy based on injection of a very high dose of nanoparticles allows to target an overwhelming majority of cells in a tumor [1]. In turn, the real advantage of introduction of nanosystems is not just accumulation in a tumor but rather implementation of a precise interaction at the level of individual cells. Thus, further progress is

Abbreviations: AMF, alternating magnetic field; BSA, bovine serum albumin; Cy5, cyanine 5; DEG, differentially expressed gene; EPR, enhanced permeability and retention; FBS, fetal bovine serum; FDR, false discovery rate; FOVs, fields of view; GFP, green florescent protein; GSEA, gene set enrichment analysis; HBSS, Hanks' Balanced Salt Solution; HO-1, heme oxygenase 1; I.v, intravenous; MNP, magnetic nanoparticle; MNPs-PEG, PEGylated MNPs based on Fe_3O_4; MNPs-pHLIP, MNPs-PEG covalently conjugated with pH low insertion peptide; PBS, phosphate buffered saline; PHLIP, pH low insertion peptide; ROS, reactive oxygen species; ScRNAseq, single-cell high-throughput RNA sequencing technique; TAMs, tumor-associated macrophages; TEM, transmission electron microscopy.

* Correspondence to: Moskovsky Trakt 2, Tomsk 634050, Russia.

E-mail addresses: allysyz@mail.ru (A.G. Pershina), efimova.lina@gmail.com (L.V. Efimova), osy_23@mail.ru (O.Y. Brikunova), nevskayaksenia@gmail.com (K.V. Nevskaya), suhininaev@mail.ru (E.V. Sukhinina), kat.hmelevsk@gmail.com (E.S. Hmelevskaya), amd2002@mail.ru (A.M. Demin), naumenko.vict@gmail.com (V.A. Naumenko), malkeyeva.dina@protonmail.com (D. Malkeyeva), elka@bionet.nsc.ru (E. Kiseleva), muhteshemka@gmail.com (A.A. Khozyainova), max89me@yandex.ru (M.E. Menyailo), d_evgeniy@oncology.tomsk.ru (E.V. Denisov), alexey.volegov@urfu.ru (A.S. Volegov), uyminm@gmail.com (M.A. Uimin), ca@ios.uran.ru (V.P. Krasnov), lm-ogorodova@mail.ru (L.M. Ogorodova).

https://doi.org/10.1016/j.nantod.2024.102300
Received 29 November 2023; Received in revised form 12 April 2024; Accepted 6 May 2024
Available online 15 May 2024

directed toward the development of more sophisticated, intelligent, and multifunctional nanosystems that move us forward to implementation of the brilliant idea about nanorobots that work *in vivo* in terms of repair and treatment [2]. At present, proposed intelligent nanoplatforms are still at initial design and optimization stages [3,4].

Magnetic nanoparticles (MNPs) owing to their magnetic properties can be heated by an alternating magnetic field (AMF) [5] or actuated by a nonheating low-frequency magnetic field [6], thereby exerting an intrinsic therapeutic effect or promoting a drug release, whereas MNP accumulation at a site of interest can be monitored by magnetic resonance imaging (MRI) [7] or magnetic particle imaging [8]. MNPs' responsiveness to an external magnetic field opens up broad opportunities for remote control and thus makes them some of the best candidates for the development of an intelligent nanosystem.

Implementation of the approach involving a precise interaction of a nanosystem with an individual cell shifts the research focus toward identification of cells that interact with nanoparticles. Despite much progress in the field [9–12], our current knowledge about interactions of nanosystems with cells in the human body are indeed limited. For the development of a nanosystem for precise therapy, a deep understanding of the nanosystem's behavior is necessary both along a journey through the body and inside a tumor. The latter is especially important because a tumor tissue is heterogeneous and, aside from cancerous cells, is composed of multiple cell types embedded in a complex extracellular matrix. The distribution of nanoparticles among (and their effect on) these cells, which are engaged in intricate crosstalk between one another, is an important topic because changes in intercellular interactions strongly influence tumor progression [13].

To address this challenge, here, we proposed an approach based on single-cell high-throughput RNA sequencing technique (scRNAseq) to reveal cell populations that interact with MNPs in a tumor and to study MNPs' effect on these cells by taking into account their affiliation with a certain cell type.

Previously, we have modified MNPs with the pH low insertion peptide (pHLIP) to create an intelligent pH-responsive system of delivery to a tumor [7]. The pHLIP acts as a smart tumor-targeting ligand owing to its ability to get inserted into the cell membrane in the acidic microenvironment found in most of solid tumors [14]. A proof-of-concept study has verified pH-dependent MNP-pHLIP accumulation in a tumor [15]. Besides, MNP-pHLIP has demonstrated biocompatibility, MRI contrast properties [7], and an ability to be heated under an AMF (Figure S1). For a comparative analysis of the behavior of the MNP-pHLIP *in vivo*, we also used nontargeting (parental) MNP-PEG nanoparticles. This comparison is relevant because the assessment of the impact of peptides (which are often included in intelligent nanosystems as a tumor-targeting ligand or as a therapeutic molecule) on *in vivo* behavior of nanomaterials contributes to the global picture of nano–bio interaction. We synthetized cyanine 5 (Cy5)-labeled PEGylated MNPs based on Fe_3O_4 (MNPs-PEG), with average size 15–18 nm and a hydrodynamic diameter of ~158 nm (Figure S2A, Table S1). The pHLIP was covalently conjugated to MNPs-PEG by analogy with [7,16], resulting in MNPs-pHLIP (Figure S2B, Table S1).

Application of scRNAseq in combination with flow cytometry, intravital microscopy, and transmission electron microscopy (TEM) made it possible to identify routes of MNPs' entry into the tumor, revealed cellular subpopulations that take up the MNPs within the tumor, and pointed to avenues of future research aimed at obtaining an effective therapeutic agent.

Results

Functionalization with peptide pHLIP affects MNP biodistribution

To understand how the MNP biodistribution changed during 48 h after intravenous (i.v.) injection, MNPs-PEG or MNPs-pHLIP were administered to mice, and 4, 24, and 48 h later, the tumor was dissected under isoflurane anesthesia, then blood, tumor, liver, lung, and spleen samples were collected for preparation of a single-cell suspension. According to whole-body epi-fluorescent imaging, MNPs-PEG or MNPs-pHLIP were already detectable in the tumor in 2 h after i.v. injection and showed a broad distribution in the body during the first 8 h; in 24 h, the fluorescent signal from nontargeted organs diminished, and MNP retention in the tumor became obvious (Fig. 1A).

According to preliminary experiments, blood circulation half-life of MNPs as determined in healthy BALB/c mice is 61.6 and 60.8 min for MNPs-PEG and MNPs-pHLIP, respectively, and fluorescence was not detectable in mouse serum at 4 h after i.v. administration (Figure S3). Nonetheless, according to flow-cytometric analysis at 4 h after the i.v. administration to 4T1 tumor–bearing mice, MNPs remained in the circulation and were associated with blood cells (Fig. 1B), mostly with monocytes and neutrophils, whereas MNPs-pHLIP also bound to B cells (Fig. 1C). Monocytes retained nanoparticles longer among other blood cells, up to 48 h. We noted that at the 4 h time point MNPs-pHLIP had approximately 4-fold higher probability of binding to blood cells than MNPs-PEG, but at 24 h this difference practically disappeared.

When analyzing the single-cell suspensions of the organs that are known to undergo well-pronounced nonspecific accumulation of MNPs, we observed a gradual increase of the MNP(Cy5)$^+$ cell fraction in the liver within 24 h with a slight decline until time point 48 h for both MNP-PEG and MNP-pHLIP groups. (Fig. 1 B) In the spleen, the highest percentage of MNP(Cy5)$^+$ cells was achieved already 4 h after injection. Immunofluorescence microscopy of liver and spleen tissue sections revealed that MNPs were colocalized with F4/80$^+$ cells (macrophages), and the observed increase in Cy5 signal intensity from time point 4 h to 24 h indicated concentration of MNPs by these cells (Fig. 1E, F). This is due to direct contact of blood with Kupffer cells localized in the lumen of liver sinusoids and splenic macrophages in the marginal zone. MNP accumulation in these organs at 24 h was confirmed by measurements of the specific magnetization (Figure S4C).

MNP(Cy5)$^+$ cells were also detected in lung tissue. Four hours after the injection, MNPs were mainly seen as colocalized with CD45$^+$F4/80$^-$ (blood) cells near blood vessels (CD31$^+$ cells, Fig. 1G, H). In 24 h, the percentage of MNP(Cy5)$^+$ cells decreased Fig. 1 B and MNPs were found sporadically within CD45$^+$F4/80$^+$ cells (macrophages) Fig. 1H. Apparently, MNPs associated with blood cells entered lungs with blood flow, but only a small proportion of MNPs extravasated in the lung tissue, where they were taken up by macrophages. Presumably, MNPs can penetrate into the lung tissue via microleakages; the formation of rare microleakages in healthy tissues has previously been described for liposomes [17]. Unlike the liver and spleen, lungs did not retain substantial amounts of MNPs. In support of this assumption, we failed to detect specific magnetization of lung tissue samples excised at 24 h after MNP administration, at least within the limits of detection of the method. Thus, the higher percentage of MNP(Cy5)$^+$ in the liver, lungs, and spleen of MNP-HLIP–treated mice in comparison to MNP-PEG–-treated ones at 4 h after injection is presumably related to a higher percentage of MNP-pHLIP–containing blood cells in the circulation.

The dynamics of MNP accumulation in the tumor tissue clearly differed from such dynamics observed in normal organs; for instance, according to flow cytometry of a single-cell suspension of tumors, the percentage of MNP(Cy5)$^+$ cells increased for 48 h after MNPs-PEG administration. The proportion of MNPs-pHLIP–containing cells in the tumor did not change over time and was lower than that determined for MNPs-PEG at 24 and 48 h after i.v. injection. Accumulation of MNPs-PEG and MNPs-pHLIP in 4T1 tumor 24 h after injection was confirmed by measurements of specific magnetization in the tumor tissue samples and through determination of the Fe content by atomic emission spectroscopy (Figure S4B, D).

MNPs penetrate into a tumor in various ways

To study extravasation routes of MNPs in a tumor

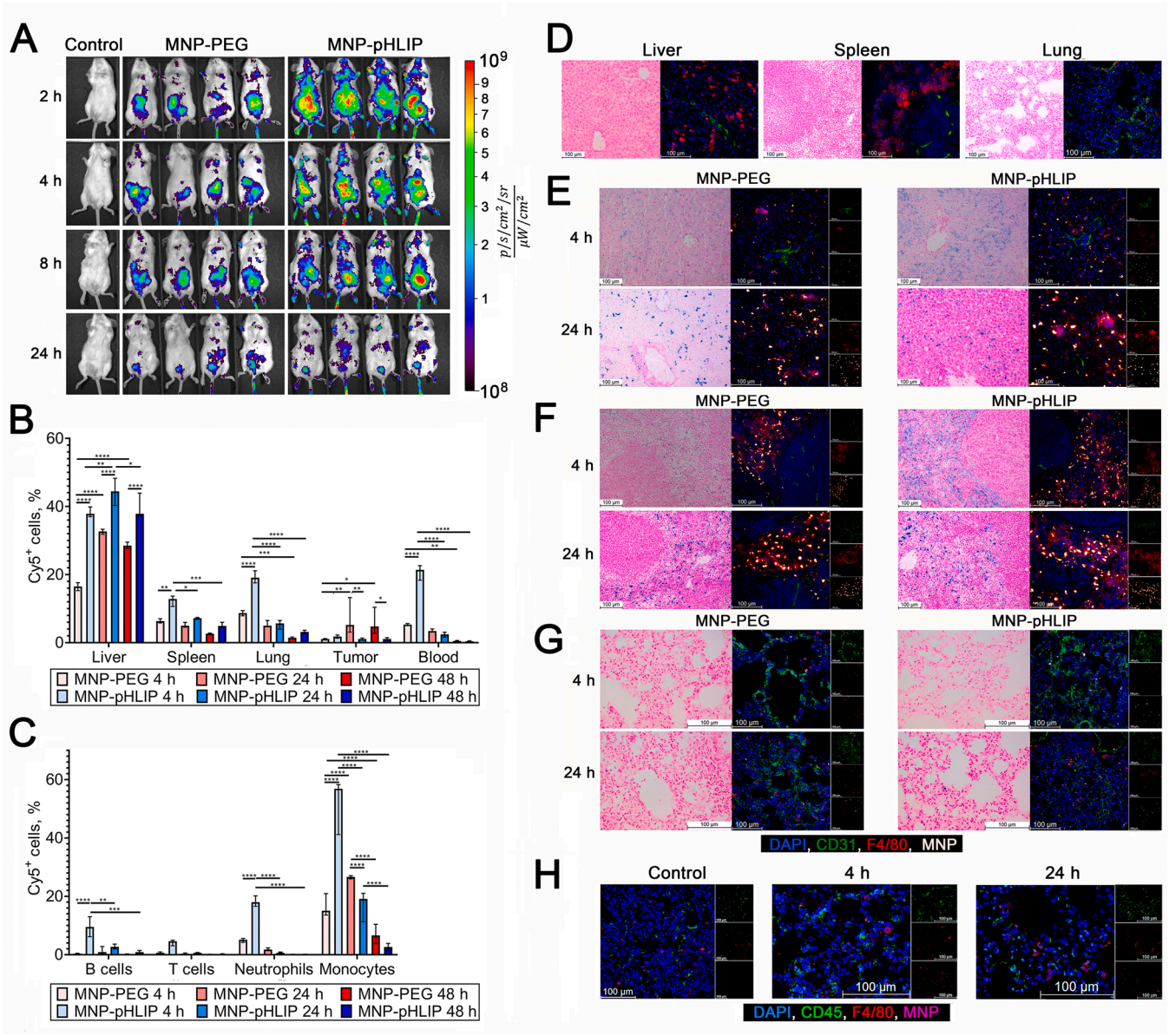

Fig. 1. Biodistribution of MNPs in 4T1 tumor–bearing BALB/c mice after i.v. injection of Cy5-labeled MNPs. (A) Whole-body epi-fluorescent imaging at the indicated time points after i.v. injection of MNPs-PEG or MNPs-pHLIP. (B) Changes in the percentage of MNP(Cy5)$^+$ cells in the tumor, blood and organs at 4, 24, and 48 h after i.v. injection of either MNPs-PEG (pale pink, pink, and red bars, respectively) or MNPs-pHLIP (pale blue, blue, and deep-blue bars, respectively) according to flow-cytometric data. (C) Changes in the percentage of MNP(Cy5)$^+$ cells in the main population of blood cells in 4T1–bearing mice at 4, 24, and 48 h after i.v. injection of MNPs-PEG (pale pink, pink, and red bars, respectively) or MNPs-pHLIP (pale blue, blue, and deep-blue bars, respectively) according to flow-cytometric data. Data are presented as a median [interquartile range]. *p < 0.05; **p < 0.01; ***p < 0.001; ****p < 0.0001, Kruskal–Wallis test followed by Dunn's multiple-comparison test. (D) Representative images of organs excised from PBS-injected mouse (control). (E) Representative images of MNP-PEG and MNP-pHLIP biodistribution in the liver, (F) spleen, (G) and lungs of 4T1 tumor–bearing BALB/c mice 4 and 24 h after i.v. administration. The tissue sections are stained with Prussian blue (on the left) or with antibodies (on the right) to CD31 (green) and F4/80 (red); MNPs are glowing. (H) Representative images of lung tissue sections excised from PBS-injected mouse (Control) and from mice 4 and 24 h after i.v. injection of MNPs-pHLIP and stained with antibodies to CD45 (green) and F4/80 (red); MNPs are magenta, nuclei are blue. Scale bars: 100 μm.

microenvironment, intravital microscopy was used. Immediately after i.v. injection of MNPs-PEG or MNPs-pHLIP, tumor vessels were counterstained, and the fluorescent signal gradually decreased during the observation time (40 min). Notably, within a few minutes upon injection, MNPs accumulated along vessel walls (Fig. 2A, Video S1). A few spots of vascular bursts were spotted along with MNP diffusion deep into tissues (Video S2); however, more often, MNPs were retained around the vessels at least for 60–90 min without penetration into tissues (Fig. 2B). These results suggested that MNPs accumulated in the perivascular area, presumably in endothelial cells. We also observed neutrophil-associated transport of MNPs to tumor tissues (Video S3). Presumably, extravasating cells can take up MNPs from the perivascular area and transfer them into the tumor core. It should be noted that there was no obvious difference in microdistribution patterns between MNPs-PEG and MNPs-pHLIP.

Supplementary material related to this article can be found online at doi:10.1016/j.nantod.2024.102300.

Four hours after i.v. administration, more than 67% of MNPs were still colocalized with blood vessels (inside or at distance <1 μm) (Fig. 3). At 24 h, the proportion of MNPs localized near CD31$^+$ cells diminished in MNP-PEG and MNP-pHLIP groups, and simultaneously, the proportion of MNPs that migrated from a blood vessel by a distance of

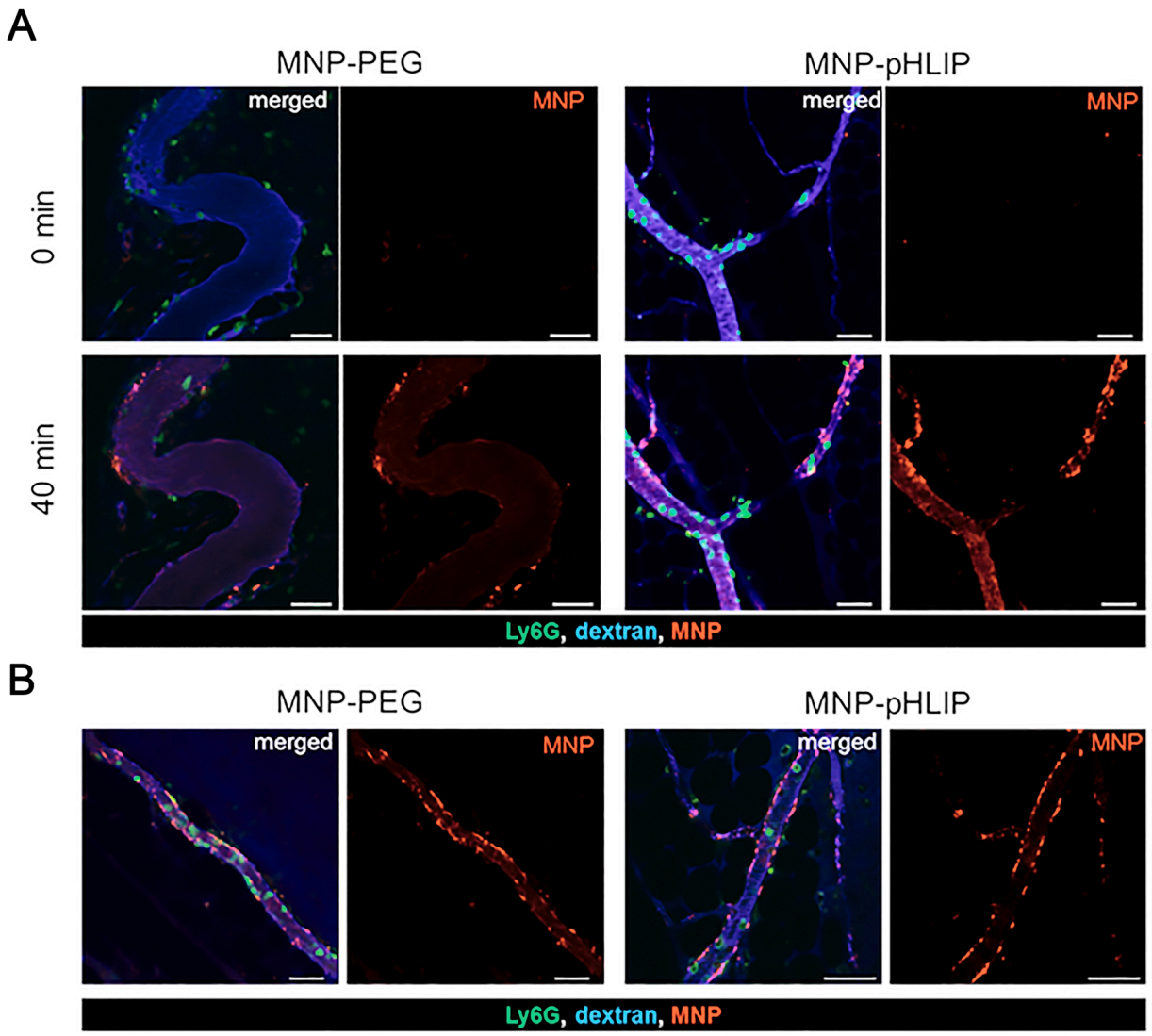

Fig. 2. *In vivo* tracking of MNPs in the tumor microenvironment. (A) Tumor blood vessels counterstained with dextran-FITC (blue) were imaged at the time and within 40 min after MNP-PEG or MNP-pHLIP i.v. injection (red); neutrophils (Ly6G) are green. Scale bar, 50 μm. (B) Accumulation of MNPs along vessel walls at 80 min after administration of MNPs-PEG or MNPs-pHLIP. Scale bar, 100 μm.

20–50 μm increased for both MNP types by more than twofold (Fig. 3, Tables S2 and S3). For MNPs-pHLIP, the proportion of MNPs found at a distance of 10–20 μm also increased. These findings clearly pointed to MNP migration from blood vessels deeper into tumor tissue during 24 h. Nonetheless, MNP(Cy5)$^{+}$CD31^{+} cells were observed at 24 h after the injection, indicating that just under half of MNPs were still retained by endothelial cells.

According to TEM ultrastructural analysis of the tumor tissue 4 h after MNP administration, we concluded that MNPs penetrate into the tumor through various routes. The MNPs were found in lysosomes of endothelial cells of capillaries and inside lysosomes of tumor cells (Fig. 4A, B) as well as in the extracellular space (Fig. 4C–E), occasionally, in close proximity to capillaries. This finding may point to the two possible routes of MNP transport through blood vessel walls. The first one is transcytosis via capillary endothelial cells: MNPs can be captured by endothelial cells and internalized via endocytosis, then the particles undergo sorting and can be either sent to lysosomes of endothelial cells for degradation or released to the extracellular space [18]. The second route is through leaks in capillaries (Fig. 4A): MNPs may leak into the extracellular space thereby avoiding endothelial cells completely. In both cases, MNPs can then be internalized by tumor cells through endocytosis [7,15] and end up in tumor cells' lysosomes (Fig. 4B).

MNPs get redistributed within the tumor

The MNPs' penetration into cells and distribution among different cell populations in a tumor was a key question in this work. To identify the population of cells that take up MNPs within the 4T1 tumor, a single-cell suspension of a tumor was stained with a set of antibodies (Table S4) and analyzed by flow cytometry. Four hours after MNP-pHLIP administration, the percentage of MNP(Cy5)$^{+}$ endothelial cells (identified as CD45^{-}CD90.2^{-}CD31^{+}) reached its maximal value and was higher as compared to the MNP-PEG–treated group (Fig. 5A); then, the percentage of MNP-pHLIP(Cy5)$^{+}$ endothelial cells decreased, indicating migration of MNPs into the tumor. At 48 h, there was no difference in the percentage of MNP(Cy5)$^{+}$ endothelial cells within the tumor between MNP-pHLIP–injected and MNP-PEG–injected mice. The percentage of MNP (Cy5)$^{+}$ neutrophils (CD45^{+}CD11b^{+}F4/80^{-}Ly6G^{+}) and especially monocytes (CD45^{+}CD11b^{+}F4/80^{-}Ly6G^{-}Ly6C^{+}) in the tumors was also relatively high during the first 24 h after MNP-pHLIP injection and declined by time point 48 h.

The MNPs-PEG manifested a gradual increase in the percentage of MNP(Cy5)$^{+}$ epithelial (cancerous) cells (CD45^{-}CD90.2^{-}CD31^{-}) during the entire observation period and showed higher accumulation in these cells in comparison with MNPs-pHLIP at 24 and 48 h after i.v.

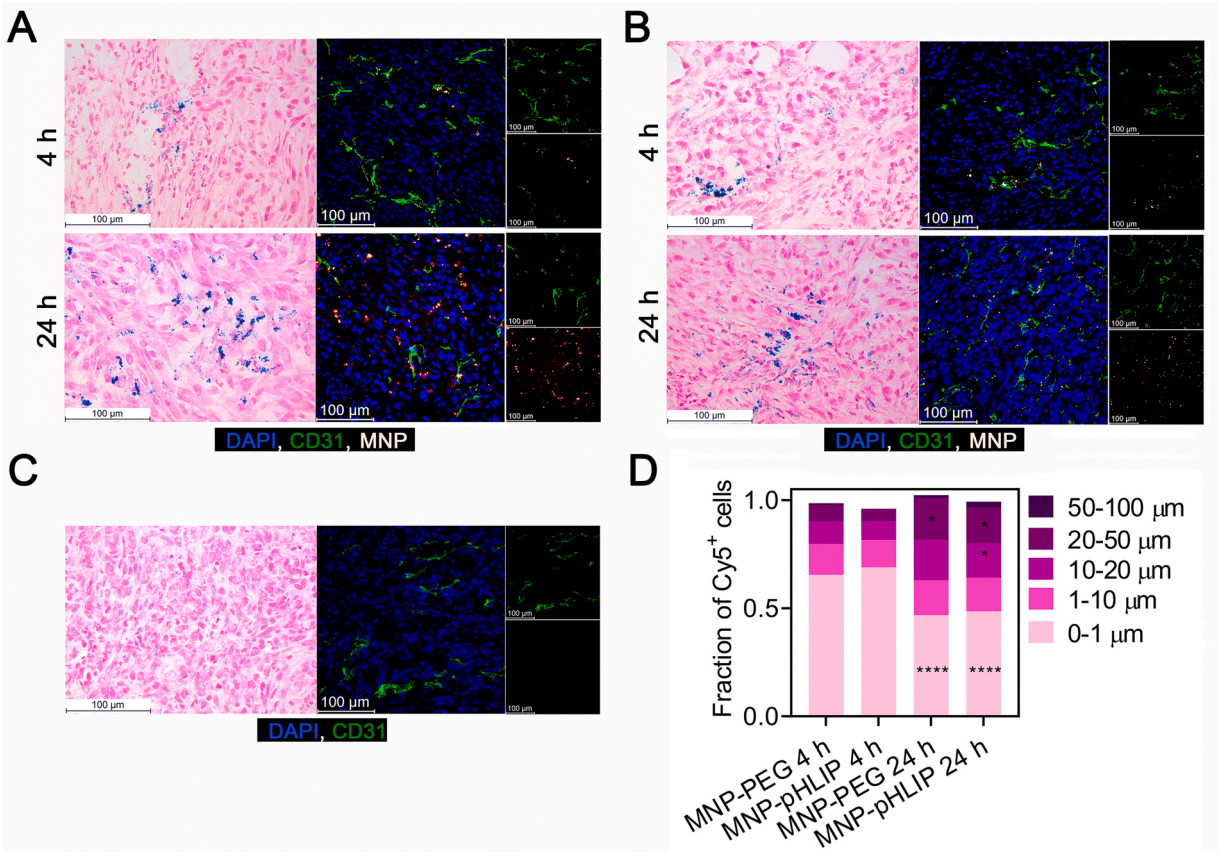

Fig. 3. Migration of MNPs from blood vessels into a 4T1 tumor. (A) Representative tumor sections excised from mice at 4 and 24 h after i.v. injection of MNPs-PEG, (B) MNPs-pHLIP or (C) PBS (Control); staining with Prussian blue (left) or antibodies to CD31 (green) (right); MNPs are glowing. (D) Proportions of MNP(Cy5)$^+$ cells migrating by a defined distance from the nearest blood vessel at 4 and 24 h after MNP-PEG or MNP-pHLIP i.v. injection according to measurements on the tumor microsections (15 fields of view [FOVs] for each sample were analyzed, and each Cy5 signal was determined separately). Data are presented as a median, n = 4. *p < 0.05; ****p < 0.0001 (in comparison with time point 4 h), Mann-Whitney U test.

administration. In turn, the percentage of MNP(Cy5)$^+$ monocytes declined from hour 4 to hour 48 in the MNP-PEG–treated group.

The presence of MNPs in CD31$^+$ endothelial cells (Fig. 5B), CD45$^+$F4/80$^-$ blood cells (Fig. 5B), and F4/80$^+$ macrophages, which were often replete with MNPs (Fig. 5B, C) was confirmed by fluorescence microscopy of freshly frozen tumor sections stained with a set of antibodies (Table S5). MNP(Cy5)$^+$CD140a$^+$ cells (fibroblasts) were found to be relatively rare and almost exclusively were detected close to blood vessels (Fig. 5D). Note that the observed colocalization of MNP (Cy5)$^+$ and CD31$^+$ signals (as calculated via the analysis of fluorescent images) may be also attributed to MNPs located in close vicinity to endothelial cells. Colocalization analysis showed that the number of MNP(Cy5)$^+$ cells in the tumor rose from hour 4 to hour 24, especially the numbers of MNP(Cy5)$^+$CD45$^+$F4/80$^-$ and MNP(Cy5)$^+$CD45$^+$F4/80$^+$ cells (Fig. 5E). This finding indicated gradual accumulation of MNPs in the tumor during 24 h, with preferential localization in macrophages and blood cells. It is important to point out that the total number of CD45$^+$F4/80$^+$ cells detected in tumor sections at 24 h after MNP-PEG and MNP-pHLIP injection became higher than this parameter at 4 h.

The increase in the percentage of MNP(Cy5)$^+$ epithelial (cancerous) cells in the tumor of MNP-PEG–treated mice during 48 h presumably was caused by the capture of MNPs from the extracellular space. In the meantime, considering the decline of the percentage of Cy5$^+$ monocytes, we hypothesized a redistribution of MNPs between cells in the tumor. To prove this hypothesis, we incubated primary human monocytes containing MNPs (MNPs-PEG or MNPs-pHLIP) with MDA-MB-231-TagGFP tumor spheroids expressing green florescent protein (GFP). After 24 h of incubation, we detected TagGFP$^+$Cy5$^+$ MDA-MB-231 cells in spheroids, thereby confirming the ability of monocytes to transfer MNPs to cancer cells (Fig. 6B). We also demonstrated this phenomenon using human-monocyte–derived tumor-associated macrophages (TAMs) and murine RAW264.7 macrophages *in vitro* in the MDA-MB-231-TagGFP and 4T1-TagGFP tumor spheroids, respectively (Fig. 6D, F). Flow-cytometric analysis showed that 20.2% ± 4.4% of 4T1-TagGFP cells in spheroids were TagGFP$^+$MNP(Cy5)$^+$ after incubation with MNP-pHLIP–containing RAW264.7 cells.

MNPs disturb the expression profile of various types of cells in the tumor

To determine the cell subsets that endocytosed MNPs in the 4T1 tumor and to elucidate the effect of MNPs on these cells, at 24 h after MNP-PEG or MNP-pHLIP i.v. administration, tumors were dissected, and each one was homogenized separately to prepare a single-cell suspension. Next, MNP-containing cells were separated from nonmagnetic cells on a MACS magnetic column placed in a MACS Separator, and scRNAseq was performed on the suspensions of MNP-containing cells; single-cell suspensions of a 4T1 tumor excised from PBS-injected mice served as a control. Graph-based analysis revealed 10 clusters, and nine of them were annotated by means of the expression of canonical gene markers of cell types (Fig. 7A, Table 1). Four major cell clusters were represented by two macrophage clusters, epithelial cells, and fibroblasts [19]. Five minor cell clusters included neutrophils, dendritic cells, endothelial cells, and T and B lymphocytes [19,20]. Relative abundance of each cell type in the 4T1 tumor samples is given in Fig. 7B.

Relative abundance of macrophages (the sum of cells in clusters 1

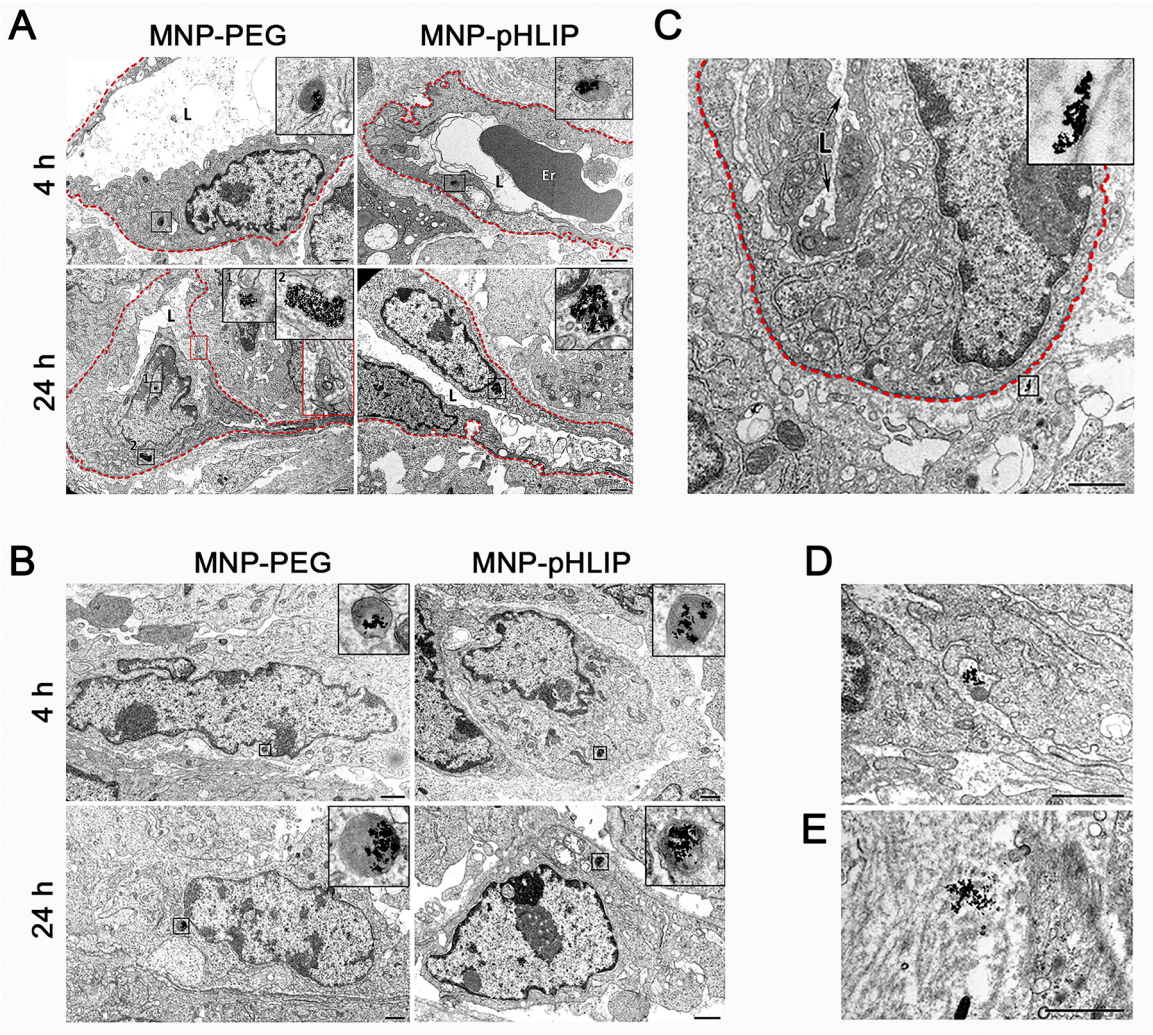

Fig. 4. TEM images of MNPs in 4T1 tumors. (A) MNPs in lysosomes of capillary endothelial cells in 4T1 tumors 4 and 24 h after MNP-PEG or MNP-pHLIP injection. The MNPs in lysosomes are shown in black rectangles, whose contents are magnified in the corners of the micrographs. The red rectangle denotes a microleak between capillary endothelial cells. The dashed red line indicates an outline of the capillary; L: capillary lumen, Er: erythrocyte. (B) MNPs in lysosomes of 4T1 tumor cells 4 and 24 h after MNP-PEG or MNP-pHLIP injection. MNPs in lysosomes are shown in black rectangles the contents of which are magnified in the corners of the micrographs. (C) MNPs-pHLIP in the extracellular space near a capillary 4 h after the injection; the particles are shown in a black rectangle, whose contents are magnified in the corner of the micrographs. The dashed red line indicates an outline of the capillary; L: capillary lumen. (D) MNPs-PEG and (E) MNPs-pHLIP in the extracellular space of the tumor at 4 h after the injection. Scale bars: 1 μm.

and 3) in groups MNP-PEG and MNP-pHLIP reached 87.95% and 72.40%, respectively, indicating preferential accumulation of MNPs in macrophages. The proportion of endothelial cells was negligible in the MNP-PEG group, but in the MNP-pHLIP group, this proportion reached 3.73% and exceeded this parameter of the control. In samples from the MNP-pHLIP group, the percentage of neutrophils was also elevated in comparison with the control. According to general clusterization, the macrophage population was divided into two clusters, discriminated based on expression of MHC II genes, *Lyve1*, and *Cd206* and presumably reflecting distinct functions of these subpopulations [21]. Table 1

Differentially expressed gene (DEG) analysis (Figure S5, S6, Supplementary Excel File 1) revealed that both types of MNPs were endocytosed by Trem2$^+$ macrophages (a subset of tumor-specific immunosuppressive macrophages). To confirm this, MNP(Cy5)$^+$F4/80$^+$Trem2$^+$ cells were detected by immunofluorescent analysis on a 4T1 tumor section (Fig. 7C); colocalization analysis showed that 36 ± 9 and 36 ± 3% of MNP(Cy5)$^+$F4/80$^+$ macrophages were Trem2$^+$ for MNP-PEG and MNP-pHLIP, respectively. The macrophages (cluster 1 and 3) in both MNP-PEG and MNP-pHLIP groups differentially expressed genes of lipid metabolism (*Apoe*, *Pld3*, *Fabp5*, and *Lgals1/3*) and of complement components (*C1qa/b/c*) [25,26]. In MNP$^+$ cells of cluster 1, the expression of MHC class II genes (*H2-Aa*, *H2-Ab1*, and *H2-Eb1*) decreased. In turn, MNP$^+$ cells of cluster 3 showed downregulation of genes of chemokines (*Ccr1*, *Ccl2/3/4/7*, and *Cxcl1/12*), interleukins (*Il1a* and *Il10*), and *H2-Aa*. *Nfkb1* was downregulated in MNP$^+$ macrophages of both clusters.

Two macrophage clusters were extracted, and a second round of dimension reduction and clustering was performed. The joint macrophage subset was further classified into M1-like, M2-like, immunoregulatory & proangiogenic, and proliferating TAMs (Fig. 7D, E, Table 1, Supplementary Excel File 2). Cluster 4 m was identified as CD14$^+$ tumor-infiltrating monocytes. Cluster 6 m was almost exclusively found in MNP-pHLIP$^+$ samples and included CD68$^+$CD14$^+$ cells with upregulated *S100a8/9*, which are known to be abundantly expressed in a subpopulation of blood monocytes participating in the recruitment and trans-endothelial migration [27]. MNP$^+$ macrophages in all clusters were *Creg1*$^+$, *Ctsd*$^+$, and *Cyba*$^+$. We believe that MNPs activated the Nrf2 pathway in TAMs (Supplementary discussion, Table S6).

MNP$^+$ epithelial (cancer) cells (cluster 2) showed signs of oxidative stress (upregulation of the *Park7* gene, an oxidative-stress sensor). This

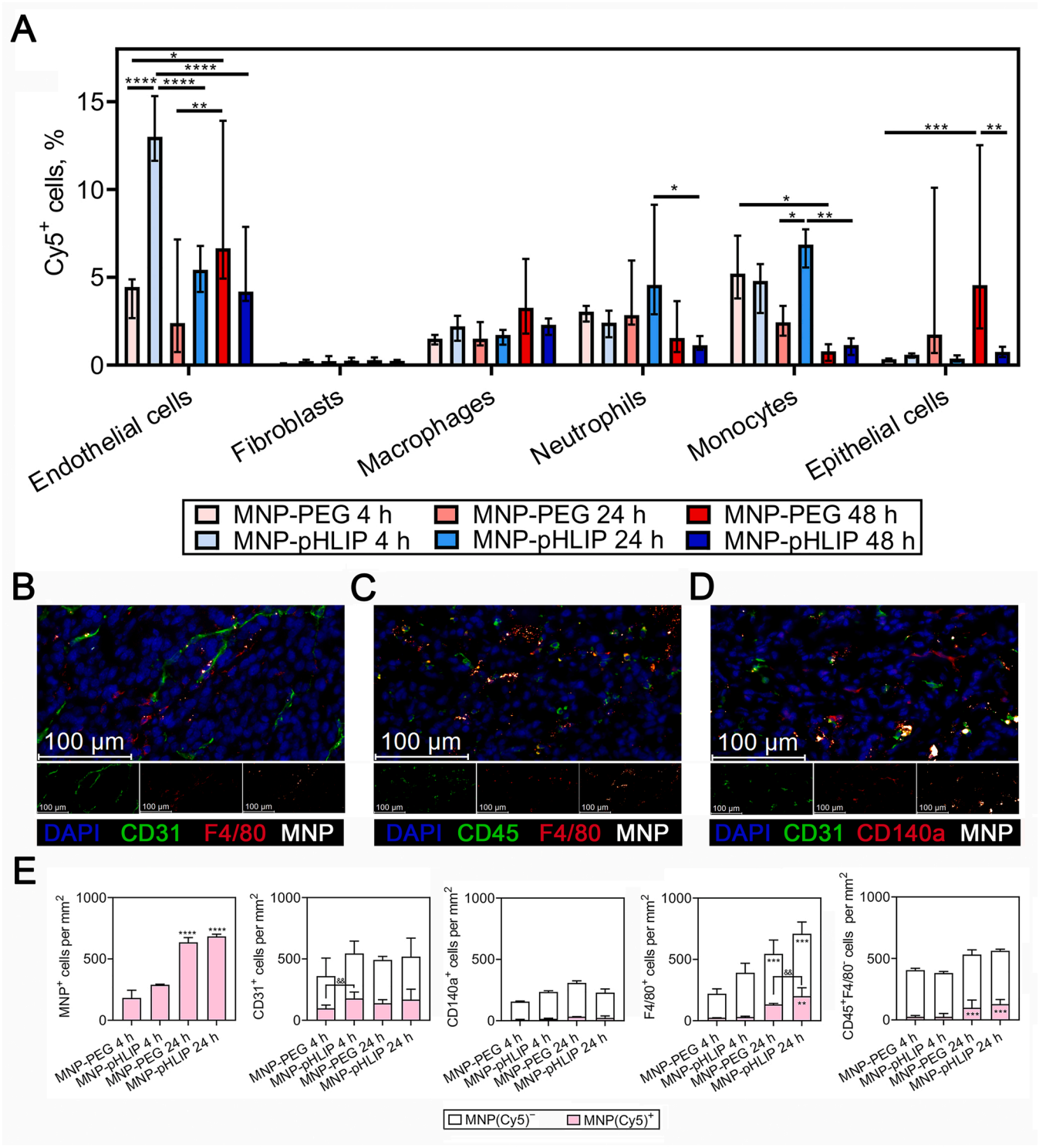

Fig. 5. The distribution of MNPs within a 4T1 tumor after i.v. injection. (A) Flow-cytometric data on the percentage of MNP(Cy5)$^+$ cells in the main populations of cells in 4T1 tumors at 4, 24, and 48 h after i.v. injection of MNPs-PEG (pale pink, pink, and red bars, respectively) or MNPs-pHLIP (pale blue, blue, and deep-blue bars, respectively). Data are presented as a median [interquartile range], n = 4. *p < 0.05; **p < 0.01; ***p < 0.001; ****p < 0.0001, Kruskal–Wallis test followed by Dunn's multiple-comparison test. (B) Representative images of tumor sections excised from mice after i.v. injection of MNPs and stained with antibodies to CD31 (green) and F4/80 (red); (C) CD45 (green) and F4/80 (red); (D) CD31 (green) and CD140a (red); MNPs are glowing. Scale bars: 100 μm. (E) Colocalization analysis of MNPs with CD31$^+$, CD45$^+$F4/80$^-$, CD45$^+$F4/80$^+$, or CD140a$^+$ cells on a tumor section obtained from mice 4 and 24 h after i.v. injection. (10 FOVs for each sample were analyzed). Data are presented as a median [interquartile range], n = 3. **p < 0.01; ***p < 0.001, ****p < 0.0001 (in comparison with time point 4 h); $^{\&\&}$ p < 0.01, Mann-Whitney U test.

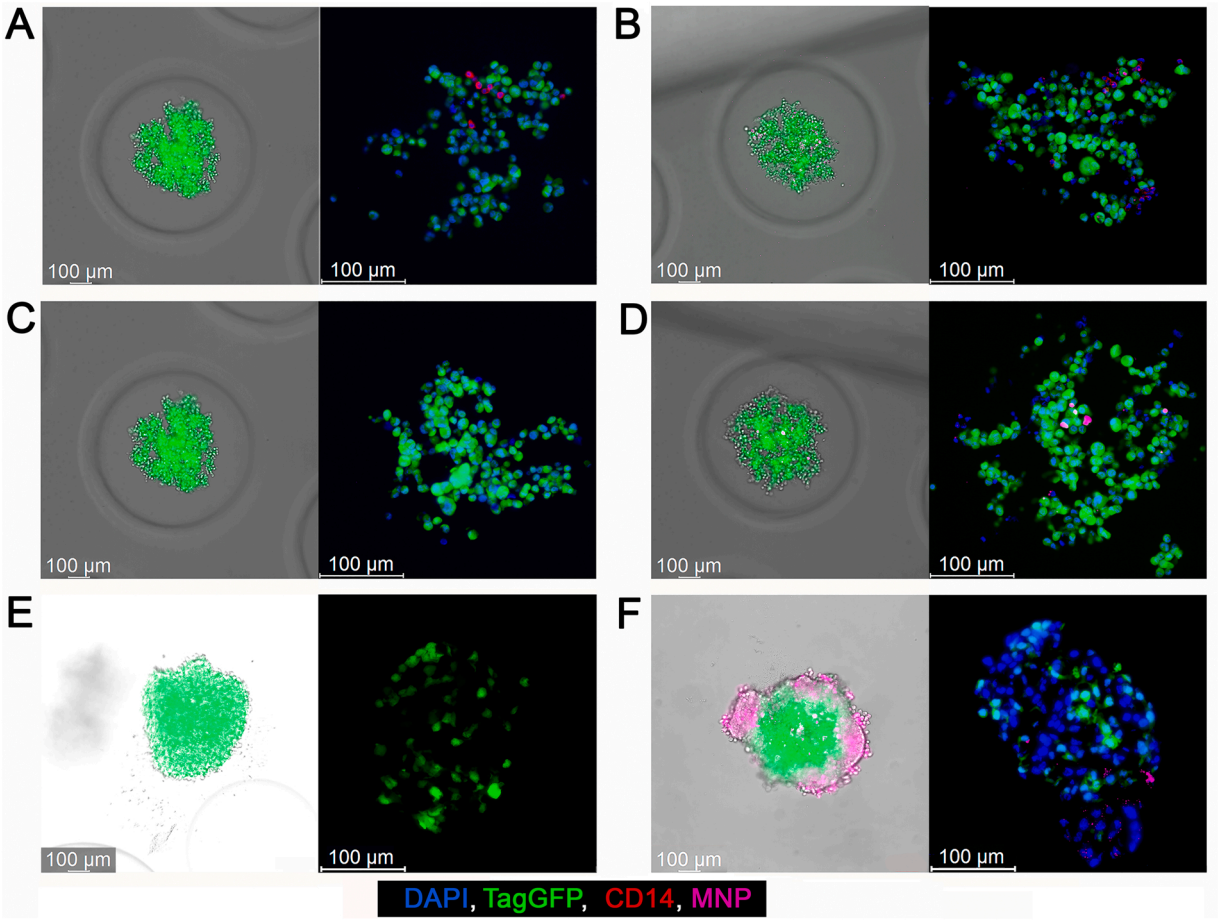

Fig. 6. Evaluation of the capacity for cell-to-cell transfer of MNPs in models of tumor spheroids. (A) Representative images of MDA-MB-231-TagGFP spheroids 24 h after incubation with intact primary human monocytes (control) or (B) with human monocytes containing MNPs-PEG, (C) intact monocyte-derived human TAMs (control), or (D) monocyte-derived human TAMs containing MNPs-pHLIP. (E) 4T1-TagGFP spheroids 24 h after incubation with intact RAW264.7 cells (control) or (F) MNP-pHLIP–containing RAW264.7 cells. The tumor cells are green, MNPs are magenta, $CD14^+$ human monocytes stained with a PE-conjugated anti-human CD14 antibody are red, and nuclei are blue. Scale bars: 100 μm.

gene encodes a redox-sensitive chaperone and protease that plays an important role in cell protection from oxidative stress and from cell death. MNP uptake by cancer cells led to a 1.5–2.0-fold increase in expression of ferritin-coding genes (*Fth1* and *Ftl1*), indicating a response to iron overload. According to gene set enrichment analysis (GSEA), MNP-pHLIP$^+$ cancer cells showed activation of the intracellular iron ion homeostasis pathway (Figure S7). Furthermore, in these cells, the *Lcn2* gene was overexpressed, which encodes the iron-trafficking protein that has been shown to block cell proliferation, migration, and invasion and to inhibit translocation of NF-κB into the nucleus [28].

MNP$^+$ cancer cells also featured upregulation of the *Hmox1* gene (fold change > 2). *Hmox1* expression is induced by a range of stimuli (e.g., hypoxia, ROS, and interleukins), and the promoter region of *Hmox1* contains binding elements for several key transcription factors (Hif-1, Nrf2, Stat3, AP-1, and NF-κB). Heme oxygenase 1 (HO-1) activity, cytoprotective in normal cells, has an antiproliferative and/or proapoptotic effect in some contexts. When HO-1 is highly expressed, the level of ferritin becomes insufficient to neutralize oxidative effects of reactive iron.

Regarding MNPs' influence on cancer cell fate, the ability to induce ferroptosis is relevant [29]. The ferroptotic role of HO-1 has been demonstrated in various tumor cell lines [30]. The *Map1lc3a* gene, upregulated in MNP$^+$ cancer cells in our experiment, encodes ubiquitin-like modifier microtubule associated protein 1 light chain 3 that is responsible for the formation of the autophagosome, activates autophagy through the ATG5–ATG7–NCOA4 pathway, and leads to ferritin degradation and thereby to intracellular unstable iron accumulation, ultimately promoting ferroptosis in fibroblasts and cancer cells [31]. In turn, upregulation of *Gpx4*, observed in MNP-pHLIP$^+$ cancer cells, can negatively affect ferroptosis by reducing phospholipid hydroperoxide [32,33].

In the case of MNPs, we propose ROS as a more plausible trigger of *Hmox1* expression. To this end, we demonstrated the ability of MNPs to induce ROS production in 4T1 cells and mouse RAW264.7 macrophages in *in vitro* experiments (Figure S8).

Analyzing DEGs in cluster 4 (annotated as fibroblasts), from the expression of genes *Mfap2*, *Tgfb1i1*, *Dcn* , and *Pdgfra*, we concluded that at least MNPs-PEG are endocytosed by subsets of extracellular-matrix–remodeling and/or myofibroblastic cancer-associated fibroblasts [34]. Of note, MNP-pHLIP$^+$ cells of cluster 4 featured upregulated genes *Abcc9* and *Kcnj8*, which are considered markers of pericytes and/or vascular smooth muscle cells [35]. Thus, this finding is in good agreement with the observed localization of MNP(Cy5)$^+$CD140$^+$ cells in close vicinity to blood vessels on the immunostained tumor sections.

MNP$^+$ cells of cluster 6 (neutrophils) showed upregulation of genes *Ccl3*, *Ccrl2*, *Gad45b*, *Il1b*, *Hcar2*, and *Nfkbia* and were recognized as activated polymorphonuclear neutrophils (myeloid-derived suppressor cells). The cells also were CD14$^+$, which is a characteristic feature of neutrophils of a tumor microenvironment [36]. Uptake of MNPs by the neutrophils provoked upregulation of some genes involved in iron ion homeostasis: *Ftl1*, *Fth1*, and *Sod2*; MNP-pHLIP$^+$ neutrophils also showed upregulation of *Slc11a1*, *Ttc7*, and *Hmox1*. The p38 MAPK-dependent

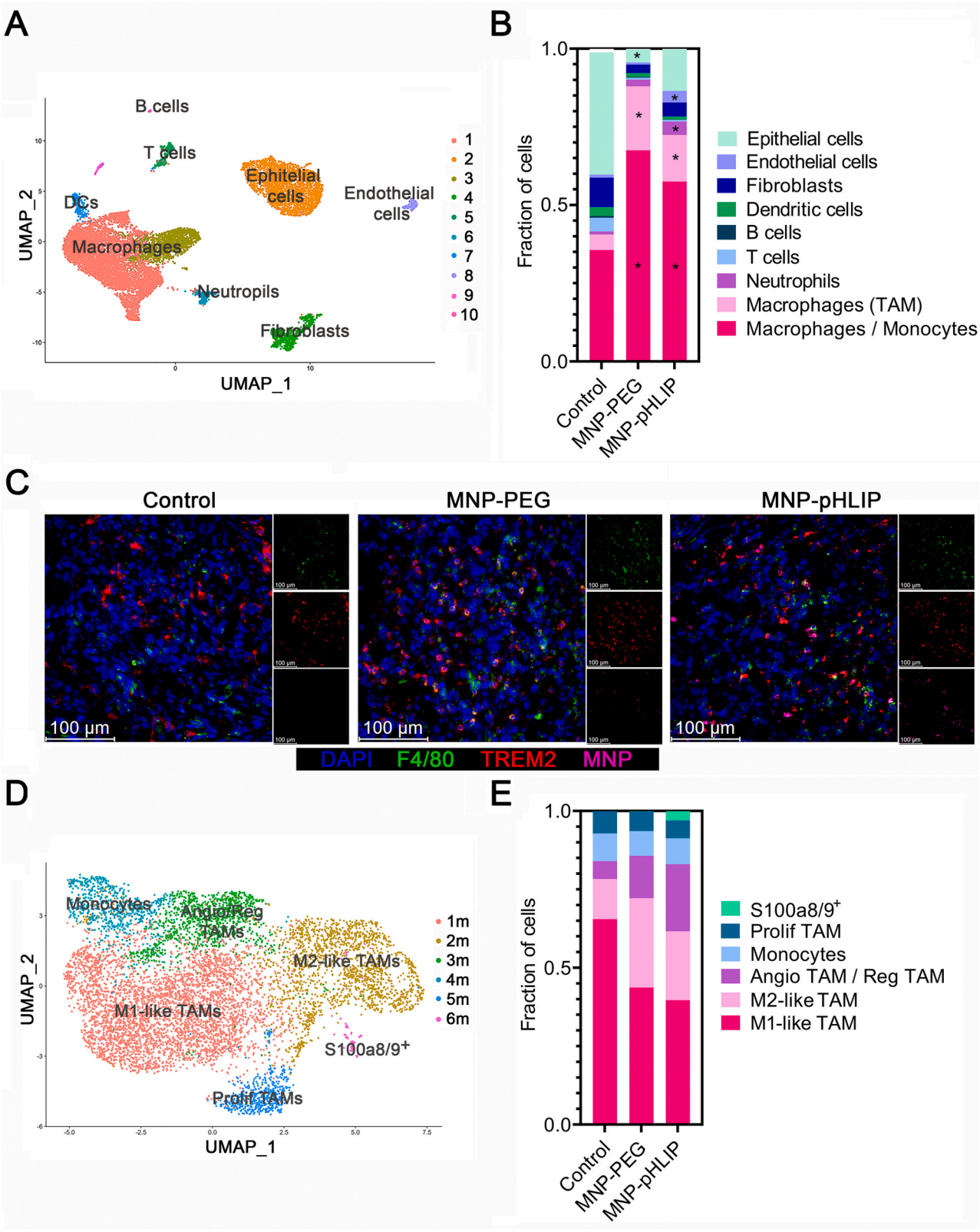

Fig. 7. The cellular landscape of the 4T1 mouse tumor. A) Uniform manifold approximation and projection (UMAP) of 12,893 cells grouped into 10 clusters. Each dot refers to a cell. The colors indicate the labels assigned to the clusters. (B) Relative abundance of each cell population in a 4T1 tumor excised from PBS-treated mice (control) and in the samples of MNP-PEG^{+} or MNP-pHLIP^{+} cells magnetically separated from 4T1 tumors that were excised from mice 24 h after MNP-PEG or MNP-pHLIP administration. DCs: dendritic cells. Data are presented as the mean, n = 2. *FDR < 0.05 (in comparison with the nonsorted control). (C) Representative tumor sections excised from mice after i.v. injection of PBS, MNP-PEG or MNP-pHLIP and stained with anti-F4/80 (green) and anti-Trem2 (red) antibodies; MNPs are magenta. Scale bars: 100 µm. (D) UMAP visualization of 4T1 tumor macrophage subclusters and (E) relative abundance of each cell subpopulation of macrophages in the groups of samples.

Table 1
Annotation of 4T1 tumor cell clusters.

Cluster	Annotation	Marker genes
Clusterization of all cells in tumor samples		
1	Macrophages / Monocytes*	*Arg1, Msr1, Cd14, Ccr5, Cx3cr1, Csf1r, Fcgr1 [Cd64], Ccr1, C1qa, C1qb, C1qc), Itgam [CD11b],* MHC II genes (*Cd74, H2-Aa, H2-Ab1, H2-Eb1, H2-DMa, H2-DMb1*)
2	Epithelial (cancerous) cells	*Epcam, Krt7, Krt8, Krt18, Cdh1*
3	Macrophages (TAMs)**	*Cd68, Selenop, Lyve1, Gas6, Mafb, Stab1*
4	Fibroblasts	*Col3a1, Col1a1, Col1a2*
5	Lymphocytes, mainly T cells	*Gzma-f, Cd3d, Cd3e, Cd3g, Cd2*
6	Neutrophils	*S100a8, S100a9, Csf3r, Retnlg*
7	Dendritic cells (antigen-presenting)	*Clec9a, Xcr1, Cd83, Cd80, Cd86, Cd209a*
8	Endothelial cells	*Cdh5, Pecam1, Tie1*
9	Other immune cells***	-
10	Lymphocytes, mainly B cells***	*Ighm, Clec12a, Flt3, Pecam1*
Sub-clusteriasation of macrophages (Cluster 1 & Cluster 3)		
1 m	$CD16^+$ / antigen-presenting (M1-like) TAMs	MHC II genes (*H2-Eb1, H2-Aa, H2-Ab, H2-DMa, Cd74*), *Cd80* and *Cd16*
2 m	M2-like TAMs	*Cd68, Adgre1, Siglec1, Cd163, Mrc1, Lyve1, Il10, Pf4, Hmox1, Ctsb/d/l, Folr2, Trem2, Ccl8*
3 m	Angio TAM / Reg TAMs	*Cd68 / Mif, Arg1, Bnip3, Adam8, Slc2a1, Mmp 9, Mmp12 / Clec4d, Pf4, Hmox1, Cd274, Spp1*
4 m	$CD14^+$ monocytes / Inflam TAMs	*Cd14, Ly6c1, Ly6c2, Inhba, Il1b, Il6, Cxcl1/2/3, Cd274, Fcgr1, Ccr2*
5 m	Prolif TAMs	*Top2a, Pclaf, Hmgb2, Stmn1, Mki67, Tubb5, Cdk1, Rrm2*
6 m	$S100a8/9^+$ (predominantly MNPs-pHLIP)	*Cd68, Cd63, Cd14, S100a8/9, Ccl2/7/8, Ifitm1, Lgals1, Pf4, Lcn1, Ftl1, Fth1, Hmox1, Lyz2*

TAM, tumor-associated macrophage; Angio, pro-angiogenic; Inflam, inflammation, Reg, immunoregulatory; Prolif, proliferating
*The cells manifested a mixed M1/M2 macrophage gene signature—we found both M2 (*Gatm*, *Apoe*, and *Ccl24*) and M1 (MHC II genes, *Cxcl3*, *Fcgr3* [*Cd16*], and *Fcgr4* [*Cd16–2*]) marker genes—had signs of macrophage activation (*Il1b*, *Tgfbi*, *Ctsc*, *Aif1*, and *PD-L1* [*Cd274*]) and reactive oxygen species (ROS) production (*Ncf2*, *Ncf4*, *Cyba*, and *Cybb*) [22,23]; a tentatively included $CD64^+CD16.2^+$ monocyte population arose from intravascular Ly-6 C^{lo} patrolling monocytes that enter the tissue [21].
**The cells expressed classic TAM marker genes and had an M2-like anti-inflammatory phenotype (DC-$SIGN^+$ [CD209], $CD163^+$, $Mrc1^+$ [CD206], $Folr2^+$, $Clec10a^+$, and $Il4ra^+$) [23,24] and expressed a broad range of chemokines (Cxcl1, Cxcl2, Cxcl10, Ccl2, Ccl7, Ccl8, and Ccl9) and immunoregulatory cytokines (IL-10, IL1-Rn, Tnf, and Vegf), and thus are involved in immune-cell recruitment and polarization.
***Clusters 9 and 10 had less than 100 cells each.

pathway, found to be activated in MNP^+ neutrophils according to GSEA (Figure S9), is critical for neutrophil chemotaxis regulation, although the effects of Erk and Jnk have not been fully elucidated yet [37].

In cluster 8, referred to as endothelial cells, MNP-$pHLIP^+$ cells differentially expressed the gene of a cytoskeletal GTP-binding protein called septin (*Sept4*), which is predicted to be involved in endo-/exocytotic processes and has been identified as an oxidative-stress factor [38].

GSEA of biological processes for up- and downregulated genes between the experimental groups for clusters 1, 3, 4, 5, 7 are shown in Figures S10-S14.

Discussion

Transport across the vascular endothelium and distribution of nanoparticles among various populations of cells in a tumor remain debatable topics [9,39]. In our study, after i.v. administration, MNPs rapidly accumulated along blood vessel walls in a tumor presumably due to the margination phenomenon [40,41]. The geometry of blood vessels, an occlusion, and microvascular bifurcations can help MNPs to adhere at certain sites more frequently [42,43], thus explaining the observed "hot spots" of MNP accumulation in tumor vessels. Next MNPs start to penetrate into the tumor.

Several mechanisms have been suggested to explain MNP penetration: the first one is entry through gaps of a leaky endothelium, allowing MNPs to enter the extracellular matrix and to be endocytosed by tumor cells within a short period after injection. In this context, the vascular bursts proposed by Kataoka and coworkers [44] match the observed macroleakages the best [17]. The second pathway is transcytosis by endothelial cells [45]. In support of this notion, MNPs-PEG and MNPs-pHLIP were found in endothelial cells by TEM and confirmed by flow cytometry and fluorescence microscopy data.

The expected third pathway (MNP migration through an opening intravascular barrier with assistance of blood cells [17])—which may be classified as paracellular or transcellular transmigration usual for leukocytes—was not directly confirmed in our study. Our data allow us to conclude only that MNPs travel in association with blood cells in the bloodstream and that MNPs localize to $CD45^+F4/80^-$ cells in 4T1 tumors. In this context, the subpopulation of cells of cluster 6 m, discovered mainly in MNP-$pHLIP^+$ tumor samples, can be regarded as a subpopulation of MNP^+ monocytes that are migrating into the tumor and starting to polarize into TAMs.

After penetration, MNPs migrated away from the blood vessels; anyway, 24 h after the injection, approximately half of the MNPs remained in close vicinity to blood vessels: in endothelial cells or in the perivascular area. Presumably, tumor extracellular-matrix stiffness can hamper the MNP migration. From this point of view, application of an AMF, which induces heating of iron oxide nanoparticles [5], might be considered a feasible approach to improving MNPs' penetration into a tumor.

In turn, blood cells may be involved in MNPs' migration from the perivascular area. This idea is supported by the following observations: (1) transfer of MNPs by neutrophils into the tumor as revealed by intravital microscopy; (2) the presence of MNP^+ neutrophils and monocytes in the tumor according to flow-cytometric data; (3) the increase in the proportion of neutrophils in the MNP-$pHLIP^+$ fraction of the tumor single-cell suspension; (4) the ability to pass MNPs from monocytes to cancer cells in the model of tumor spheroids. The general ability of monocytes to take up MNPs-PEG and MNPs-pHLIP by endocytosis within no more than 1 h was demonstrated in our previous study [16]. The observed accumulation of MNP$(Cy5)^+$ neutrophils and monocytes in tumors during first 24 h with a simultaneous decrease in the MNP$(Cy5)^+$ cell number in the bloodstream—more pronounced for MNPs-pHLIP—may reflect their possible role in MNP penetration into the tumor.

The major population of MNP^+ cells in tumors was resident TAMs. More specifically, MNPs prefer to accumulate in $Trem2^+$ TAMs. Lately, targeting of $TREM2^+$ TAMs has been proposed as a strategy to enhance tumor immunotherapy [46]. Thus, further progress could be made through conjugation of MNPs with, for example, therapeutic RNAs for

reprogramming the TAMs by analogy with ref. [47].

Conjugation with the pHLIP affected MNP biodistribution *in vivo* and increased chances to bind to blood cells, primarily neutrophils and monocytes. Concerning the tumor tissue, MNPs-pHLIP more often and/or rapidly entered into endothelial cells; however, this preference did not give any benefit. The best explanation for this observation is that at neutral pH, the pHLIP peptide is known to be located at the surface of the cell membrane [48], and conjugation with MNPs may hamper washing away from the membrane via the normal perfusion proposed for the free peptide owing to the MNP-pHLIP margination effect.

The presence of the peptide on MNPs' surface raises a legitimate question about nonequivalence of the protein coronas formed on the MNP-PEG and MNP-pHLIP surface after injection into the bloodstream [49,50] as a cause of the observed discrepancy. In our previous paper, we could not detect a clear difference between the repertoires of proteins identified in MNPs-PEG and MNPs-pHLIP coronas arising in human serum [16]. In the abovementioned experiment, taking into account complicated architecture of a protein corona [51], we used magnetic separation of MNPs during sample preparation in order to preserve proteins of a soft corona [52]. Thus, the observed difference in biodistribution between MNP-PEG and MNP-pHLIP is likely explained by an interaction of the pHLIP itself with the cells' surface.

Conclusions

Concerning the MNPs' *in vivo* behavior, we revealed that MNPs penetrate into a tumor via various routs: at least through vascular burst and endothelial transcytosis. Further migration of MNPs within the tumor core may be assisted by blood cells, likely neutrophils and monocytes. It was shown that monocytes are able to transfer MNPs to cancer cells. The conjugation of MNPs with the pHLIP favored their interaction with tumor endothelial cells and blood cells in the circulation, thereby influencing MNP biodistribution, but did not improve cancer cell targeting.

By implementing an approach based on scRNAseq, we determined the cell populations that endocytosed MNPs in the 4T1 tumor and revealed preferential accumulation of MNPs in regulatory $Trem2^+$ TAMs. We also noticed that cells recognize MNPs as a stressor: MNPs activated the Nrf2 pathway in TAMs and the intracellular iron ion homeostasis pathway in cancerous cells as well as facilitated ROS production in cells. Further research is proposed that is aimed at stimulating MNPs' penetration into a tumor by AMF and at designing an approach to precise manipulation of $Trem2^+$ macrophages in order to promote antitumor immunity.

A major advantage of the scRNAseq based approach (over antibody-assisted techniques, such as flow cytometry and fluorescence microscopy) is unbiased identification of populations of the cells that take up nanoparticles, with simultaneous detection of an influence of nanoparticles on expression patterns that determine biological function of the cells. The proposed approach can be also adapted to nonmagnetic nanoparticles, for example, fluorescent nanoparticles could be separated by fluorescence-activated cell sorting. Our results, focused on nanoparticle–cell interaction in tumor-bearing mice, should contribute to the global picture of nano–bio interaction and to the development of engineered nanoparticles for biomedicine.

Methods

MNP synthesis. Silica-coated iron oxide nanoparticles (Fe_3O_4) modified with (3-aminopropyl)trimethoxysilane) (Sigma) were synthetized according to procedure described earlier [53]. For preparing fluorescent MNPs, 3-aminopropyl)trimethoxysilane was conjugated beforehand with Cy5 NHS ester (Lumiprobe). Next, MNPs were covalently modified with heterobifunctional *O*-[*N*-(6-maleimidohexanoyl) aminoethyl]-*O*′-[3-(*N*-succinimidyloxy)-3-oxopropyl]polyethylene glycol (molecular weight ~3000, Sigma-Aldrich) (PEG3000) to obtain MNPs-PEG. The pHLIP (ACEQNPIYWARYADWLFTTPLLLLDLALLVDADEGT, Pepmic) [7,16] was covalently attached to MNPs-PEG. Immobilization of PEG3000 and pHLIP molecules on MNPs was confirmed by IR spectroscopy data (Figure S2C, D). MNPs-PEG and MNPs-pHLIP possess high saturation magnetization (M_s) (Table S1). The characterization of MNPs is given in Supplementary materials (Figure S2, Table S1).

The cell line. Mouse macrophages RAW264.7, mouse mammary carcinoma 4T1 cells (ATCC), and MDA-MB-231 human adenocarcinoma cells (ECACC) were grown at 5% CO_2 and 37 °C in the complete DMEM/F12 (Gibco) medium supplemented with 10% (v/v) of fetal bovine serum (FBS) (Gibco), 1% of GlutaMax (Gibco), and 1% of PenStrep (Gibco).

Human monocytes and monocyte-derived TAMs. Monocytes were isolated from a leukocyte/thrombocyte concentrate purchased from the Siberian Federal Research and Clinical Centre (Seversk, Russia) according to a procedure described in ref. [16]. To obtain human monocyte-derived TAMs, we used a published protocol [54] with a minor modification. In brief, $CD14^+$ monocytes were incubated for 5 days in the serum-free X-VIVO medium (Lonza) supplemented with 10 ng/mL macrophage colony-stimulating factor (M-CSF, ProSpec, USA), 10^{-8} M dexamethasone (KRKA, Slovenia), and 10% of a culture supernatant of MDA-MB-231 cells (cultivated for 36 h in DMEM/F12 with 2% of FBS and passed through a 0.22 μm Millex-GV Filter, Millipore, France).

Animal experiments. These experiments were conducted in compliance with the Guide for the Care and Use of Laboratory Animal Resources (1996) and approved by the Bioethics Committee of the Siberian State Medical University (decision No. 5891 of 26 June 2018).

Five-week-old female BALB/c mice were purchased from the SPF vivarium of the Institute of Cytology and Genetics, the Siberian Branch of the Russian Academy of Sciences.

For tumor induction, 10^6 4T1 cells in 50 μL of Phosphate Buffered saline (PBS, Sigma) were injected into the right inguinal mammary gland of the mice. The tumors were allowed to develop for 10 days. At the beginning of the experiments, the tumor volume was 134 ± 33 mm^3.

MNPs resuspended in ~200 μL of PBS (2 mg/mL) were i.v. injected (via a tail vein) into mice (20 (mg [Fe])/kg); the administration rate was 200 μL per minute. Mice in control groups were injected with PBS.

Intravital microscopy. Tumor intravital microscopy was performed as described previously [17]. In brief, the tail vein of anesthetized mice was cannulated, and fluorescently labeled antibodies Ly6G-BV421 (clone 1A8, 0.6 μg; Biolegend) and CD11b-PE (clone M1/70, 0.6 μg; Biolegend) were injected to stain host cells *in vivo*. FITC-labeled 2MDa dextran (100 μg, Sigma-Aldrich) was injected to counterstain the vessels. Tumor vasculature was studied at the moment of and within 40–80 min after the injection of Cy5-labeled MNPs-PEG or MNPs-pHLIP (54 μg per mouse in terms of iron concentration). Images were captured at the acquisition rate of 1.5 frame/min using a Nikon A1R inverted confocal microscope (Japan).

Blood and tissue sampling. For sample collection, the mice were anesthetized with 2% isoflurane (EZ-7000–320, Braintree scientific), and the anesthetic level was checked by foot pinch using forceps. After tumor dissection, blood samples were collected via cardiac puncture into EDTA-containing tubes. Next, the lungs, liver, and spleen were dissected and weighed.

Pharmacokinetic analysis. For this analysis, healthy BALB/c mice were i.v. injected with MNPs at a final dose of 4 (mg [Fe])/kg. Blood samples were collected in 5, 30, 60, 120, and 240 min and 24 h after the injection, the tubes with blood were kept at room temperature for 30 min to allow the blood to clot. Then, 200 μL of serum was placed in a black 96-well plate, and fluorescence intensity was measured on a Cary Eclipse Fluorescence Spectrometer (Agilent).

Immunofluorescence. For fluorescence microscopy, tumor samples were fresh-frozen in Tissue-Tek® O.C.T. Compound (Sakura Finetek, USA) in liquid-nitrogen–cooled isopentane immediately after dissection. The frozen tumor samples were cryosectioned on an HM525 NX Cryostat

(Thermo Fisher Scientific). The tissue sections were placed on poly-L-lysine–coated slides (Menzel), fixed with 4% paraformaldehyde for 15 min, and stained using a set of antibodies. Briefly, slides were washed 3 times with PBS, then with PBS supplemented with 0.1% of Tween 20 for 30 s, and blocked in 3% bovine serum albumin (BSA) in PBS for 60 min. The slides were stained with a solution of a primary antibody in 3% BSA in PBS at 4 °C overnight and with a secondary antibody at room temperature for 45 min (Table S5). Nuclei were stained using Mounting Medium With DAPI, Aqueous, Fluoroshield (Abcam).

Fluorescence microscopy images were captured with a Leica DFC9000 GT sCMOS camera under a Leica DMi8 microscope (Germany). In each sample, 10–15 FOVs were analyzed. The distance was measured using Leica LasX software. For colocalization analysis, the multichannel images were input into the Colocalization_Image_Creator plugin of the ImageJ freeware (Fiji) [55].

Histology. Fresh-frozen tumor samples were sliced and stained with the Prussian Iron Stain Kit (Abcam).

TEM analysis. This analysis of the tumor samples was carried out according to the procedure reported in ref. [56].

Preparation of single-cell suspensions of organs. For preparation of a liver cell suspension, liver samples were incubated with 120 U of collagenase II (PanEco) in complete DMEM/F12 for 40 min, and cells were filtered through 70 μm cell strainer (STEMCELL Technologies, Inc.). For lung cell analysis, lung samples were digested with collagenase I (255 U) for 2 h and then filtered through 40 μm cell strainer. To produce a spleen cell suspension, spleen samples were passed through 40 μm cell strainer in complete DMEM/F12.

Preparation of tumor single-cell suspensions. After tumor dissection, the tissue samples were immediately cut into small pieces with a scalpel on ice and placed into 1.5 mL of the complete DMEM/F12 medium on ice. For dissociation of tumor cells, 600 U of collagenase Type IV (Gibco) in 500 μL of Hanks' Balanced Salt Solution (HBSS, Gibco) was added, and the samples were incubated at 137 rpm and 37 °C for 2 h. After that, 2 mL of cold PBS and 1 mL of Trypsin-EDTA (PanEco, Russia) were introduced, and the samples were mixed and incubated for 1 min. Next, 8 mL of cold PBS and 250 U of DNase I (Roche) in 500 μL of HBSS were added into the tubes and incubated for 2 min, and the cell suspension was filtered through a 70 μm cell strainer (STEMCELL Technologies Inc.). The cells were pelleted by centrifugation at 300 × *g* for 10 min at 4 °C and resuspended in FACS or MACS buffer.

Flow cytometry. Before staining, tumor cells were incubated with an Fc blocker (TruStain FcX™ anti-mouse CD16/32, Biolegend) for 10 min in FACS buffer (3% FBS with 1 mM EDTA in PBS). After staining with an antibody cocktail, the cells were washed with PBS twice and resuspended in 100 μL of PBS. The blood samples (100 μL) were lysed with ACK buffer (150 mM NH_4Cl, 10 mM $KHCO_3$, 0.1 mM EDTA, pH 7.2–7.4) after staining. The full list of antibodies used is given in Tables S4 and S7.

Flow cytometer Cytoflex (Beckman Coulter) was used for analyses. The gating strategy for flow cytometry data analysis was as follows: a SSC vs FSC density plot gate was applied to identify a population of cells. Then, doublet discrimination was performed by plotting FSC-H vs FSC-A; for tumor samples, this step was followed by plotting SSC-H vs SSC-A. Next, dead cells were excluded by means of a viability dye DAPI (4',6-diamidino-2-phenylindole), propidium iodide or SYTOX Green. Single staining was performed to set up compensation controls, and fluorescence minus one controls were employed to determine positive-negative thresholds in multicolor immunofluorescent experiments. Representative gating strategies for a cell population in tumor samples are provided in Figure S15 and for blood samples in Figure S16.

Representative gating strategies for the MNP(Cy5)$^+$ population in liver, spleen, and lung samples are provided in Figure S17.

MNP$^+$ cell sorting. The sorting strategy was based on magnetic properties of the cells containing MNPs. A tumor single-cell suspension (10^7 cells/mL) without any antibody addition was loaded onto an LS Column (Miltenyi Biotec) that was placed in a magnetic rack, then the column was washed 3 times, and cells were eluted with 1 mL of MACS buffer (0.5% BSA with 0.1 mM EDTA in PBS) (Figure S18). Finally, cells were centrifuged and resuspended in PBS without Ca^{2+} Mg^{2+} with 5% FBS.

Single-cell sequencing. A single-cell suspension was diluted in PBS containing 0.04% of BSA by pipetting with wide-bore pipette tips, and placed on the ice. Cell counting was carried out on a Countess II automated cell counter (Thermo Fisher Scientific, USA) with 0.4% trypan blue (Thermo Fisher Scientific, USA). The concentration of cell stocks was ~1000 cells/μl. Single-cell cDNA libraries were prepared using the 10x Genomics Chromium Controller (10x Genomics, USA) and the Single Cell 3′ Reagent Kit v3.1 (Dual Index) (10x Genomics, USA) following the standard manufacturer's protocol. Approximately 8300 cells from each sample were loaded onto the Chromium Controller to recover 5000 cells for library preparation and sequencing. The concentration of cDNA libraries was measured by means of the dsDNA High Sensitivity Kit on a Qubit 4.0 fluorometer (Thermo Fisher Scientific, USA). The quality of cDNA libraries was assessed using High Sensitivity D1000 ScreenTape on a 4150 TapeStation (Agilent, USA). The resultant cDNA libraries were pooled, denatured, and sequenced on Genolab M (GeneMind Biosciences, China) using pair-end reads (28 cycles for read 1, 90 cycles for read 2, 10 cycles for the i7 index, and 10 cycles for the i5 index).

Bioinformatic analysis. Samples were mapped to a reference genome (mouse reference genome, mm10) in CellRanger v6.1.1 (10x Genomics, Pleasanton, CA, USA). Parameter "–include-introns" was used. The Seurat software package version 4.3.0 was employed for quality control and analysis of the data from the single-cell high-throughput RNA sequencing. We generated six Seurat objects and then filtered these Seurat objects to exclude low-quality cells. The filtering parameters are presented in Table S8. After that, we excluded mitochondrial genes from the analysis. Then, a list of Seurat objects was created for integration, and normalization was performed using SCTransform separately for each sample. We applied the RunPCA function to conduct principal component analysis (PCA). After PCA, the RunHarmony function of Harmony package version 0.1.1 was utilized to integrate the Seurat object. PCA of integrated samples was performed, and 20 principal components were used for cell clustering (resolution = 0.25). UMAP was then applied to visualize the cell atlas [57].

Cluster markers were found using the FindAllMarkers function. The identification of cell types was performed manually and by means of SingleR package version 2.0.0.

DEGs were next processed in RStudio (R version 4.1.0) [58]. The Ggplot2 software package was used for visualization of DEGs [59]. The genes with an adjusted $p < 0.05$ and $\log_2$ fold change > 0.5 were designated as DEGs. GSEA was performed with R package clusterProfiler [60].

In total, we sequenced 36283 cells, with an average of 6047 cells per sample, and detected an average of 18825 genes per cell.

For compositional single-cell data analysis, scCODA [61] was applied. The scCODA assessment was conducted using the 'Dendritic cells' category as the reference cell type (FDR < 0.1). Additionally, we determined the significance of effects on cell types that were mostly independent of the reference. By sequentially running scCODA and selecting each cell type as a reference once, we next used a majority vote to find cell types that significantly changed (FDR < 0.05) more than half the cases.

The *in vitro* model of cell-to-cell transfer of MNPs. 4T1-TagGFP and MDA-MB-231-TagGFP monoclonal cell lines expressing GFP were obtained by lentivirus transduction using LVT-TagGFP2 (Evrogen, Russia) according to a standard protocol. 4T1-TagGFP and MDA-MB-231-TagGFP tumor spheroids were generated in a 2% agarose mold cast using a silicon micro-mold (MicroTissues Inc., USA).

Pre-adhered cells (RAW 264.7 or monocyte-derived human TAMs) were incubated with MNPs-PEG or MNPs-pHLIP (20 μg/mL) for 4 h in a CO_2 incubator.

Human monocytes were incubated with MNPs-PEG or MNPs-pHLIP (20 μg/mL) on a rotator for 1 h at 37 °C, washed with PBS twice by centrifugation, and placed on a tissue culture plate for adhesion for 24 h. The cells in control samples were incubated without MNPs.

Next, MNPs were completely discarded, and the adherent cells were vigorously washed with PBS. RAW 264.7 cells and monocytes were detached from the culture plates using TrypLE (Gibco, UK); monocyte-derived human TAMs were detached on ice. Two thousand MNP^+ RAW264.7 cells were added to 4T1-TagGFP spheroids (composed of 8000 cells), 30,000 MNP^+ human monocytes or monocyte-derived human TAMs were added to MDA-MB-231-TagGFP spheroids (81 spheroids in a mold formed from 150,000 cells) and incubated for 24 h in the CO_2 incubator.

Finally, the spheroids were fixed with 4% paraformaldehyde, embedded into OCT, frozen in liquid nitrogen, and next cryosectioned and stained with DAPI. Monocytes were stained with a PE-conjugated anti-human CD14 antibody (M5E2, Biolegend). Additionally, 4T1-TagGFP spheroids were dissociated into a single-cell suspension and analyzed by flow cytometry.

Statistical analyses. These analyses were performed in GraphPad Prism (GraphPad Software). The data were evaluated for normality by the Shapiro–Wilk test. Differences between continuous variables with a normal distribution were assessed by two-way ANOVA followed by Tukey's multiple-comparison *post hoc* test. Differences between non-normally distributed variables were assessed by unpaired Mann-Whitney U test or by the Kruskal–Wallis test followed by Dunn's multiple-comparison test. Data with *P* values below 0.05 were considered statistically significant.

Funding

This work was supported by the Centre for Strategic Planning of the Federal Medical-Biological Agency of Russia [contract numbers No. 0373100122119000033 of 07 June 2019 and No. 0373100122120000041 of 04 June 2020].

CRediT authorship contribution statement

Elena Kiseleva: Investigation. **Mikhail A Uimin:** Investigation. **Maxim E. Menyailo:** Investigation. **Anna A. Khozyainova:** Investigation. **Victor P. Krasnov:** Supervision. **Evgeny V. Denisov:** Supervision. **Kseniya V Nevskaya:** Investigation. **Lina V. Efimova:** Investigation. **Ludmila M. Ogorodova:** Supervision. **Alexandra Pershina:** Writing – review & editing, Writing – original draft, Supervision, Project administration, Methodology, Investigation, Conceptualization. **Ekaterina V Sukhinina:** Investigation. **Alexander M. Demin:** Writing – original draft, Investigation. **Olga Y Brikunova:** Investigation. **Ekaterina S. Hmelevskaya:** Investigation. **Dina Malkeyeva:** Writing – original draft, Investigation. **Aleksey S Volegov:** Investigation. **Victor A. Naumenko:** Writing – original draft, Investigation.

Declaration of Competing Interest

The authors declare that they have no known competing financial interests or personal relationships that could have appeared to influence the work reported in this paper.

Data Availability

Data will be made available on request.

Acknowledgements

The synthesis and characterization of the nanoparticles were carried out within a state assignment IOS UB RAS (topic No. 124020500044–4 and 124020500044–9) using the equipment of multi-access center Spectroscopy and Analysis of Organic Compounds at Postovsky Institute of Organic Synthesis, the Ural Branch of the Russian Academy of Sciences. The TEM was performed at the Multi-Access Center for Microscopic Analysis of Biological Objects (ICG SB RAS, Novosibirsk, Russia) (FWNR-2022–0015). The single-cell RNA library preparation and sequencing were carried out on the equipment of the core facility Medical Genomics (Tomsk NRMC).

Appendix A. Supporting information

Supplementary data associated with this article can be found in the online version at doi:10.1016/j.nantod.2024.102300.

References

[1] B. Ouyang, W. Poon, Y.N. Zhang, Z.P. Lin, B.R. Kingston, A.J. Tavares, Y. Zhang, J. Chen, M.S. Valic, A.M. Syed, P. MacMillan, J. Couture-Senécal, G. Zheng, W.C. W. Chan, The dose threshold for nanoparticle tumour delivery, Nat Mater. 19 (12) (2020) 1362–1371, https://doi.org/10.1038/s41563-020-0755-z. PMID: 32778816.
[2] X. Kong, P. Gao, J. Wang, Y. Fang, K.C. Hwang, J. Hematol. Oncol. 16 (2023) 74.
[3] M. Saeed, J. Gao, Y. Shi, T. Lammers, H. Yu, Theranostics 9 (2019) 7981–8000.
[4] R. Cheng, H.A. Santos, Adv. Health Mater. 12 (2023) e2202063.
[5] A.M. Demin, A.V. Vakhrushev, A.G. Pershina, M.S. Valova, L.V. Efimova, A. A. Syomchina, M.A. Uimin, A.S. Minin, G.L. Levit, V.P. Krasnov, V.N. Charushin, Int J. Mol. Sci. 23 (2022).
[6] Y.I. Golovin, S.L. Gribanovsky, D.Y. Golovin, N.L. Klyachko, A.G. Majoug, A. M. Master, M. Sokolsky, A.V. Kabanov, J. Control. Release 129 (2015) 43–60.
[7] A.M. Demin, A.G. Pershina, A.S. Minin, O.Y. Brikunova, A.M. Murzakaev, N. A. Perekucha, A.V. Romashchenko, O.B. Shevelev, M.A. Uimin, I.V. Byzov, D. Malkeyeva, E. Kiseleva, L.V. Efimova, S.V. Vtorushin, L.M. Ogorodova, V. P. Krasnov, ACS Appl. Mater. Interfaces 13 (2021) 36800–36815.
[8] T.M. Buzug, G. Bringout, M. Erbe, K. Gräfe, M. Graeser, M. Grüttner, A. Halkola, T. F. Sattel, W. Tenner, H. Wojtczyk, J. Haegele, F.M. Vogt, J. Barkhausen, K. Lüdtke-Buzug, Z. Med Phys. 22 (2012) 323–334.
[9] W.C.W. Chan, BME Front. 4 (2023) 0016.
[10] L.A. Lane, Appl. Phys. Rev. 7 (2020).
[11] M. Kumar, P. Kulkarni, S. Liu, N. Chemuturi, D.K. Shah, Adv. Drug Deliv. Rev. 194 (2023) 114708.
[12] P. MacMillan, A.M. Syed, B.R. Kingston, J. Ngai, S. Sindhwani, Z.P. Lin, L.N. M. Nguyen, W. Ngo, S.M. Mladjenovic, Q. Ji, C. Blackadar, W.C.W. Chan, Nano Lett. 23 (2023) 7197–7205.
[13] K.E. de Visser, J.A. Joyce, Cancer Cell 41 (2023) 374–403.
[14] O.A. Andreev, D.M. Engelman, Y.K. Reshetnyak, Mol. Membr. Biol. 27 (2010) 341–352.
[15] A.G. Pershina, O.Y. Brikunova, A.M. Demin, M.A. Abakumov, A.V. Vaneev, V. A. Naumenko, A.S. Erofeev, P.V. Gorelkin, T.R. Nizamov, A.R. Muslimov, A. S. Timin, D. Malkeyeva, E. Kiseleva, S.V. Vtorushina, I.V. Larionova, E.A. Gerenga, A.S. Minin, A.M. Murzakaev, V.P. Krasnov, A.G. Majougad, L.M. Ogorodova, Nanomed.: Nanotechnol., Biol., Med. 32 (2021) 102317.
[16] A.G. Pershina, A.M. Demin, P. N.A, B. O.Y, L.V. Efimova, K.V. Nevskaya, A. V. Vakhrushev, V.G. Zgoda, M.A. Uimin, A.S. Minin, D. Malkeyeva, E. Kiseleva, A. P. Zima, V.P. Krasnov, L.M. Ogorodova, Colloids Surf. B: Biointerfaces 221 (2023) 112981.
[17] V.A. Naumenko, K.Y. Vlasova, A.S. Garanina, P.A. Melnikov, D.A. Potashnikova, D. A. Vishnevskiy, S.S. Vodopyanov, V.P. Chekhonin, M.A. Abakumov, A.G. Majouga, ACS Nano 13 (2019) 12599–12612.
[18] V.M. Pulgar, Front Neurosci. 12 (2019) 1019.
[19] X. Liu, M. Bai, H. Li, P. Ye, X. Duan, C. Wu, Z. Huang, S. Lu, J. Zhang, Z. Zhao, F. Guo, R. You, W. Qin, W. Wang, A. Han, L. Shen, Y. Wang, Z. Zhao, H. Luo, J. Wu, J. Front Immunol. 13 (2022) 965342.
[20] W. Feng, L. Chen, P.K. Nguyen, S.M. Wu, G. Li, Front Cardiovasc Med 6 (2019) 165.
[21] J. Schyns, Q. Bai, C. Ruscitti, C. Radermecker, S. De Schepper, S. Chakarov, F. Farnir, D. Pirottin, F. Ginhoux, G. Boeckxstaens, F. Bureau, T. Marichal, Nat. Commun. 10 (2019) 3964.
[22] P. Murray, T. Wynn, Nat Rev Immunol, 11 (201) 723–737.
[23] L. Chávez-Galán, M.L. Olleros, D. Vesin, I. Garcia, Front Immunol. 6 (2015) 263.
[24] J. Korbecki, K. Kojder, D. Simińska, R. Bohatyrewicz, I. Gutowska, D. Chlubek, I. Baranowska-Bosiacka, Int. J. Mol. Sci. 21 (2020) 8412.
[25] D. Khantakova, S. Brioschi, M. Molgora, Vaccin. (Basel) 10 (2022) 943.
[26] S.Z. Wu, G. Al-Eryani, D.L. Roden, S. Junankar, K. Harvey, A. Andersson, A. Thennavan, C. Wang, J.R. Torpy, N. Bartonicek, T. Wang, L. Larsson, D. Kaczorowski, N.I. Weisenfeld, C.R. Uytingco, J.G. Chew, Z.W. Bent, C.-L. Chan, V. Gnanasambandapillai, C.-A. Dutertre, L. Gluch, M.N. Hui, J. Beith, A. Parker, E. Robbins, D. Segara, C. Cooper, C. Mak, B. Chan, S. Warrier, F. Ginhoux, E. Millar, J.E. Powell, S.R. Williams, X.S. Liu, S. O'Toole, E. Lim, J. Lundeberg, C.M. Perou, A. Swarbrick, Nat. Genet 53 (2021) 1334–1347.
[27] I. Eue, B. Pietz, J. Storck, M. Klempt, C. Sorg, Int Immunol. 12 (2000) 1593–1604.
[28] M. Feng, J. Feng, W. Chen, W. Wang, X. Wu, J. Zhang, F. Xu, M. Lai, Mol. Cancer 15 (2016) 77.
[29] C. Bae, H. Kim, Y.-M. Kook, C. Lee, C. Kim, C. Yang, M.H. Park, Y. Piao, W.-G. Koh, K. Lee, Mater. Today Bio 17 (2022) 100457.

[30] K.N. Luu Hoang, J.E. Anstee, J.N. Arnold, Front Immunol. 12 (2021) 658315.
[31] H. Li, X. Zhang, C. Yi, Y. He, X. Chen, W. Zhao, D. Yu, BMC Cancer 21 (2021) 835.
[32] S.K. Chiang, S.E. Chen, L.C. Chang, Int J. Mol. Sci. 20 (2018) 39.
[33] M. Sacher, A. Di Bacco, V.V. Lunin, Z. Ye, J. Wagner, G. Gill, M. Cygler, Proc. Natl. Acad. Sci. USA 102 (2005) 18326–18331.
[34] D. Lavie, A. Ben-Shmuel, N. Erez, R. Scherz-Shouval, Nat. Cancer 3 (2022) 793–807.
[35] K. Ando, L. Tong, D. Peng, E. Vázquez-Liébanas, H. Chiyoda, L. He, J. Liu, K. Kawakami, N. Mochizuki, S. Fukuhara, J. Grutzendler, C. Betsholtz, Dev. Cell 57 (2022) 1383–1399.e1387.
[36] F. Veglia, A. Hashimoto, H. Dweep, E. Sanseviero, A. De Leo, E. Tcyganov, A. Kossenkov, C. Mulligan, B. Nam, G. Masters, J. Patel, V. Bhargava, P. Wilkinson, D. Smirnov, M.A. Sepulveda, S. Singhal, E.B. Eruslanov, R. Cristescu, A. Loboda, Y. Nefedova, D.I. Gabrilovich, J. Exp. Med 218 (2021).
[37] X. Liu, B. Ma, A.B. Malik, H. Tang, T. Yang, B. Sun, G. Wang, R.D. Minshall, Y. Li, Y. Zhao, R.D. Ye, J. Xu, Nat. Immunol. 13 (2012) 457–464.
[38] K. Neubauer, B. Zieger, Front Cell Dev. Biol. 9 (2021) 768409.
[39] Q. Lin, P. Fathi, X. Chen, EBioMedicine 59 (2020) 102958.
[40] E. Carboni, K. Tschudi, J. Nam, X. Lu, A.W. Ma, AAPS PharmSciTech 15 (2014) 762–771.
[41] R. Toy, E. Hayden, C. Shoup, H. Baskaran, E. Karathanasis, Nanotechnology 22 (2011) 115101.
[42] E.J. Carboni, B.H. Bognet, D.B. Cowles, A.W.K. Ma, Biophys. J. 114 (2018) 2221–2230.
[43] S. Wang, T. Ye, G. Li, X. Zhang, H. Shi, PLoS Comput. Biol. 17 (2021) e1008746.
[44] Y. Matsumoto, J.W. Nichols, K. Toh, T. Nomoto, H. Cabral, Y. Miura, R.J. Christie, N. Yamada, T. Ogura, M.R. Kano, Y. Matsumura, N. Nishiyama, T. Yamasoba, Y. H. Bae, K. Kataoka, Nat. Nanotechnol. 11 (2016) 533–538.
[45] B.R. Kingston, Z.P. Lin, B. Ouyang, P. MacMillan, J. Ngai, A.M. Syed, S. Sindhwani, W.C.W. Chan, ACS Nano 15 (2021) 14080–14094.
[46] M. Binnewies, J.L. Pollack, J. Rudolph, S. Dash, M. Abushawish, T. Lee, N. S. Jahchan, P. Canaday, E. Lu, M. Norng, S. Mankikar, V.M. Liu, X. Du, A. Chen, R. Mehta, R. Palmer, V. Juric, L. Liang, K.P. Baker, L. Reyno, M.F. Krummel, M. Streuli, V. Sriram, Cell Rep. 37 (2021) 109844.
[47] K.V. Nevskaya, A.G. Pershina, E.S. Hmelevskaya, L.V. Efimova, M.K. Ibragimova, D.S. Dolgasheva, I.A. Tsydenova, A.A. Ufandeev, E.E. Buyko, E.A. Perina, K. A. Gaptulbarova, E.A. Kravtsova, S.V. Krivoshchekov, V.V. Ivanov, A.M. Guriev, E. V. Udut, N.V. Litviakov, J. Med Chem. (2024).
[48] O.A. Andreev, A.G. Karabadzhak, D. Weerakkody, G.O. Andreev, D.O. Engelman, Y.K. Reshetnyak, PNAS 107 (2010) 4081–4086.
[49] M.P. Monopoli, C. Åberg, A. Salvati, K.A. Dawson, Nat. Nanotechnol. 7 (2012) 779–786.
[50] K.A. Dawson, Y. Yan, Nat. Nanotechnol. 16 (2021) 229–242.
[51] Y. Zhang, J. Wu, J. Lazarovits, W. Chan, J. Am. Chem. Soc. 142 (2020) 8827–8836.
[52] D. Baimanov, J. Wang, J. Zhang, K. Liu, Y. Cong, X. Shi, X. Zhang, Y. Li, X. Li, R. Qiao, Y. Zhao, Y. Zhou, L. Wang, C. Chen, Nat. Commun. 13 (2022) 5389.
[53] A.M. Demin, A.V. Maksimovskikh, A.V. Mekhaev, D.K. Kuznetsov, A.S. Minin, A. G. Pershina, M.A. Uimin, V.Y. Shur, V.P. Krasnov, Ceram. Int. 47 (2021) 23078–23087.
[54] I. Larionova, A. Kiselev, E. Kazakova, T. Liu, M. Patysheva, P. Iamshchikov, Q. Liu, D.M. Mossel, V. Riabov, M. Rakina, A. Sergushichev, N. Bezgodova, S. Vtorushin, N. Litviakov, E. Denisov, P. Koshkin, D. Pyankov, M. Tsyganov, M. Ibragimova, N. Cherdyntseva, J. Kzhyshkowska, Front Immunol. 14 (2023) 1000497.
[55] A. Lunde, J.C. Glover, Sci. Rep. 10 (2020) 19027.
[56] A.G. Pershina, O.Y. Brikunova, A.M. Demin, O.B. Shevelev, I.A. Razumov, E. L. Zavjalov, D. Malkeyeva, E. Kiseleva, N.V. Krakhmal', S.V. Vtorushin, V. L. Yarnykh, V.V. Ivanov, R.I. Pleshko, V.P. Krasnov, L.M. Ogorodova, Nanomed.: Nanotechnol., Biol. Med. 23 (2020) 102086.
[57] A.A. Khozyainova, A.A. Valyaeva, M.S. Arbatsky, S.V. Isaev, P.S. Iamshchikov, E. V. Volchkov, M.S. Sabirov, V.R. Zainullina, V.I. Chechekhin, R.S. Vorobev, M. E. Menyailo, P.A. Tyurin-Kuzmin, E.V. Denisov, Biochem. (Mosc.) 88 (2023) 231–252.
[58] R. Team, RStudio: Integrated Development for R, RStudio, PBC, Boston, MA 2020.
[59] H. Wickham, ggplot2: Elegant Graphics for Data Analysis [Internet], Springer-Verlag New York, 2016.
[60] T. Wu, E. Hu, S. Xu, M. Chen, P. Guo, Z. Dai, T. Feng, L. Zhou, W. Tang, L. Zhan, X. Fu, S. Liu, X. Bo, G. Yu, Innov. (Camb.) 2 (2021) 100141.
[61] M. Büttner, J. Ostner, C.L. Müller, F.J. Theis, B. Schubert, Nat. Commun. 12 (2021) 6876.